Lawrence Berkeley National Laboratory
Laboratory Directorate

Title
Extended radiation source imaging with a prototype Compton imager

Permalink
https://escholarship.org/uc/item/75r4n1j5

Journal
Applied Radiation and Isotopes, 67(4)

ISSN
0969-8043

Authors
Sullivan, John P
Tornga, Shawn R
Rawool-Sullivan, Mohini W

Publication Date
2009-04-01

DOI
10.1016/j.apradiso.2008.11.007

Peer reviewed

Extended radiation source imaging with a prototype Compton imager

John P. Sullivan [a,*], Shawn R. Tornga [b], Mohini W. Rawool-Sullivan [c]

[a] MS B244, Los Alamos National Laboratory, Los Alamos, NM 87545, USA
[b] MS D466, Los Alamos National Laboratory, Los Alamos, NM 87544, USA
[c] MS B230, Los Alamos National Laboratory, Los Alamos, NM 87544, USA

ABSTRACT

This paper reports results from a prototype Compton imager (PCI) which consists of three planes of silicon pixel detectors as a scattering detector followed by an array of CsI(Tl) crystals as an absorbing detector. The CsI(Tl) array is mounted directly behind the silicon detectors. Simple back-projection algorithms are not sufficient to resolve extended shapes, but iterative algorithms provide the necessary de-convolution. List-mode maximum likelihood expectation maximization (LM-MLEM) is an iterative algorithm that reconstructs the most probable source distribution for a given data set. LM-MLEM attempts to reconstruct an image by finding successive approximations to the true source data. Each data set imaged is different, but the number of iterations required for convergence is typically 10–30 for the PCI. In this paper, reconstructed images of point and extended sources using measured PCI data are presented. Data are corroborated using GEANT4 simulations.

© 2008 Elsevier Ltd. All rights reserved.

1. Introduction

In counter terrorism and other similar applications it is necessary to detect special nuclear materials (SNM) as well as other sources with weak radiation signatures. The detection problem is further complicated by natural radiation, the typically minimal measurement time available (so the flow of commerce is not inhibited), distance factors, legitimate shipments of radioactive sources/materials, and consumer products containing naturally-occurring radioactive materials. Imaging detectors are frequently tested using point sources—both because these reveal the inherent angular resolution of the detector and because point sources are readily available in most laboratories. However, in the real world many of the sources of interest are larger than the angular resolution of a detector. Measuring the size and shape of such an "extended source" is important for many applications of an imaging detector. To gain better understanding of this problem in the laboratory setting a prototype Compton imager (PCI) was constructed at the Los Alamos National Laboratory (LANL). This paper reports results obtained using the PCI. These results are corroborated with the GEANT4 simulations. In particular, this paper shows reconstructed images of extended sources in addition to point sources.

A number of Compton imagers have been constructed in the past. A group from Japan uses silicon strip detectors (Takeda et al., 2007; Odaka et al., 2007) combined with CdTe detectors—their intended application is astrophysics. Vetter and his co-workers have worked with double-sided silicon strip and germanium detectors (Mihailescu et al., 2007; Vetter et al., 2007). A group in Michigan has investigated 3D CdZnTe Compton cameras (Lehner et al., 2004). The Naval Research Laboratory has designed an imager based on thick silicon strip detectors (Kurfess et al., 2007). Kanbach et al. (2005) use double-sided silicon strip detectors with CsI(Tl) calorimeter in their Compton/Pair telescope. Llosa et al. (2008) have built a prototype detector intended for use in nuclear medicine which uses silicon pixels and large NaI detectors. Other than Llosa et al. (2008), none of these gamma-ray imaging projects use pixilated silicon detectors as we do—and the reconstruction algorithms of Llosa et al. (2008) are significantly different than ours since the energy of the source is known in advance. The use of pixilated silicon detectors has also been proposed for positron imaging in nuclear medicine (Park et al., 2007) by a team which included many of the authors of Llosa et al. (2008). The pixilated silicon detectors used in the PCI, which provide adequate position resolution for the scattering detectors, are one of the differences between this work and previous work. The use of CsI scintillators, which have moderate resolution, but are relatively cheap and easy to operate, also distinguishes this imager from most others. In addition, the use of room temperature detectors distinguishes this work from some of the previous work. There have not been many attempts to reconstruct extended sources using Compton imaging. The exceptions are Motomura et al. (2007), who reconstructed extended biological sources (which do not have well-defined

shapes which are known in advance) using a germanium-based detector, Zoglauer (2005) who reconstructed a ring source, and Vetter et al. (2007) who reconstructed a line source using germanium detectors. Here, we have used a combination of silicon pixels and scintillators as a detector and have reconstructed two extended sources with well-defined shapes, one of which has a significant width, in addition to reconstructing point sources.

2. The PCI

The PCI, an imaging system based on the Compton interaction of gamma-rays, uses three planes of silicon pixel detectors as a scattering detector followed by an array of CsI(Tl) crystals as an absorbing detector. These detectors are referred to as the "silicon" and "CsI" detectors in the following text. Since this detector has been described in a previous publication (Rawool-Sullivan et al., 2008) only the more relevant details will be given here. Each silicon plane consists of a 16×20 array of $0.3\,\text{cm} \times 0.3\,\text{cm}$ silicon pixels (Li, 2001). The silicon detectors are $280\,\mu\text{m}$ thick and are glued onto circuit boards which contain the readout electronics (Ideas, 2004). Behind the silicon planes is a 6×7 detector element array of $1.2\,\text{cm} \times 1.4\,\text{cm} \times 1.0\,\text{cm}$ CsI(Tl) crystals, each with an attached silicon PIN diode. Circuit boards holding the preamplifiers for the CsI detector readout are behind the CsI array (St. Gobain, 2003). Both the silicon and the CsI detectors are enclosed in light-tight housings. All events with a simultaneous (within ~2 μs) signal in at least one silicon pixel and one CsI detector were collected. In the reconstruction of events, it is assumed that a photon Compton scatters in the silicon "scattering" detectors and is absorbed in the CsI "absorbing" detector. The sum of the energies in the two detectors is assumed to be the energy of the incident gamma-ray.

For these measurements, the size of the CsI crystals is the dominant contribution to the angular resolution. The spacing between scattering detectors and the absorbing detector used for the measurements represents a compromise between angular resolution (better if the detectors are farther apart) and detection efficiency or field of view (which are both better if the detectors are closer together). The Si layers were 2.7 cm apart and the distance between the center of the last Si plane and the center of the CsI crystals was 6.1 cm. GEANT4 simulations (Agostinelli et al., 2003) were set-up using this same PCI geometry. These simulations included the GEANT low-energy Compton scattering (GLECS) package (Kippen, 2004) an extension to GEANT4 that more accurately models atomic binding effects for low-energy Compton and Rayleigh scattering. The use of GLECS is needed to include "Doppler broadening" (Kippen, 2004; Riberfors, 1975) in the simulations. Based on experimental measurements, the resolution of the silicon detectors in simulations was assumed to be independent of energy with a full-width half-maximum (FWHM) of 36 keV. The resolution of the CsI detectors in simulations (also based on experimental measurements) is given in (1), where E is the photon energy in keV.

$$FWHM = \sqrt{(12.5\,\text{keV})E + \left(\frac{E}{13.7}\right)^2} \tag{1}$$

Eq. (1) gives, for example, 119 keV FWHM (14.2%) for $E = 834$ keV. When used without the CsI detectors in the trigger logic, the silicon resolution was somewhat better (typically 16–24 keV FWHM), however, the time "jitter" in the CsI + silicon coincidence logic signal resulted in the observed 36 keV silicon resolution. A diagram of the PCI set-up is shown in Fig. 1.
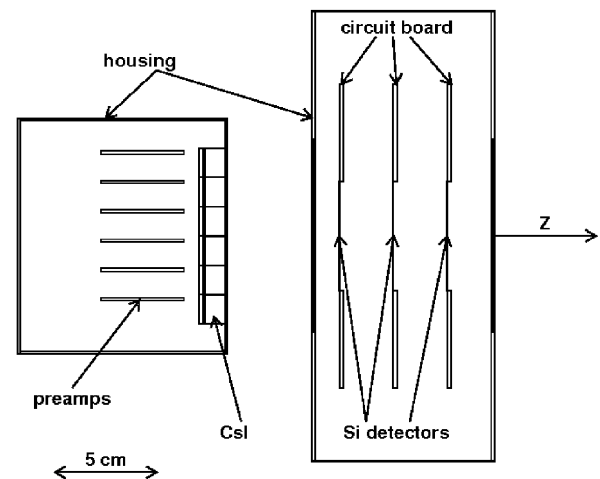

Fig. 1. A diagram of the PCI (viewed from the top) showing the silicon detectors, the CsI crystals, the circuit boards used for silicon readout, the preamplifier boards in the CsI readout, and the detector housings. The photodiodes attached to the CsI crystals are shown as small, unlabeled, boxes to the left of the CsI crystals. The coordinate system used in the analysis has a Z axis (shown as an arrow in the sketch) which passes through the center of the detectors and whose origin ($Z = 0$) is at the outer surface (right-most in the diagram) of the silicon detector housing. In this sketch the X axis points toward the top of the page and the Y axis points out of the page toward the reader. The gamma-ray sources are normally placed "in front" of the detector—meaning on the right side of this diagram. This diagram is drawn to scale. A 5 cm scale is shown.

3. Back-projection reconstruction

Reconstruction of Compton scatter data relies on the calculation of the scattering angle from the Compton formula. The basic Compton scatter formula is shown in (2).

$$\cos\theta = 1 - mc^2 \left[\frac{1}{E_{CsI}} - \frac{1}{E_\gamma} \right] \tag{2}$$

In (2) the incident gamma-ray energy (E_γ) is the sum of the energy deposited by the scattered electron in the silicon (E_{Si}) and the energy deposited by scattered photon in the CsI (E_{CsI}) and mc^2 is the mass of the electron in energy units.

A sample interaction is sketched in Fig. 2. The Compton scatter angle is defined relative to the vector ($\boldsymbol{u} = (u_x, u_y, u_z)$) pointing from the location at which the secondary photon was stopped to the location of the initial Compton scatter of the photon. The exact location of the interaction within a PCI detector element is unknown, therefore, the interaction is assumed to have taken place at the center of the silicon pixel. The interaction in the CsI detector element is assumed to have taken place at center of the detector element in the transverse directions (X and Y in our coordinate system) and at the most probable interaction depth—which is a function of the photon energy and is calculated using the interaction lengths in Berger et al. (2005). The initial gamma-ray's direction should fall somewhere on the surface of the cone with a central axis defined by vector $\boldsymbol{u}$, an opening angle (θ) defined by the Compton scatter formula (2), and with an apex at the position of the photon scatter in the silicon detector. Because the direction of the Compton-scattered electron is not measured, the correct azimuthal angle (ϕ) within the cone is unknown—so during reconstruction every value of ϕ from 0 to 2π is treated as equally likely. To use the geometry of this cone effectively, it must be rotated into the "lab" coordinate system used in the image analysis—which has its Z axis passing through the center of the detector (Fig. 1). Without going into further details, the set of vectors which define the cone start at the apex of the cone (i.e. at the silicon pixel in which the photon is assumed to have scattered)

with directions defined by the vector $\mathbf{v} = (v_x, v_y, v_z)$ calculated using the matrix multiplication in (3)—where ϕ is any value from 0 to 2π.

$$\begin{bmatrix} v_x \\ v_y \\ v_z \end{bmatrix} = \begin{bmatrix} \cos\theta_u \cos\phi_u & -\sin\phi_u & \sin\theta_u \cos\phi_u \\ \cos\theta_u \sin\phi_u & \cos\phi_u & \sin\theta_u \sin\phi_u \\ -\sin\theta_u & 0 & \cos\theta_u \end{bmatrix} \begin{bmatrix} \sin\theta \cos\phi \\ \sin\theta \sin\phi \\ \cos\theta \end{bmatrix} \tag{3}$$

In (3), θ_u and φ_u are the angles associated with the vector $\mathbf{u}$. Specifically, if $R_{CsI} = (X_{CsI}, Y_{CsI}, Z_{CsI})$ is the location of the CsI detector in which the Compton-scattered photon stopped, and $R_{Si} = (X_{Si}, Y_{Si}, Z_{Si})$ is the location of the silicon pixel in which the primary photon scattered, then, $\mathbf{u} = (X_{Si}-X_{CsI}, Y_{Si}-Y_{CsI}, Z_{Si}-Z_{CsI})$ and the angles θ_u and ϕ_u are calculated from the elements of the vector $\mathbf{u}$ (e.g. $\cos\theta_u = u_z/|u|$ and $\phi_u = \tan^{-1}(u_y/u_x)$). Each of the vectors corresponding to a specific value of ϕ is individually transformed to the lab frame by the rotation in (3), and then projected onto multiple planes at different source-to detector distances, which are used to try to reconstruct an image.

All back-projected cones should intersect at a common point, revealing the source position. Fig. 3 shows the sequence of back-projected cones for a simulated ^{137}Cs point source located at

$(X = 0.0\,\text{cm}, Y = 0.0\,\text{cm}, Z = 10.0\,\text{cm})$, where Z (see Fig. 1) is the distance from the silicon detector housing to the source. The source position becomes evident after a sufficient number of cones intersect.

The algorithm used to construct the back-scattered image has some "cuts" to select events which improve the image quality. The data are collected using the coincidence trigger in the PCI hardware, which requires a signal in one or more silicon detector pixels and one or more CsI detector. These are referred to as "recorded events." The first step in the image processing is to select events which have signals in exactly one silicon pixel and exactly one CsI detector. This is done to eliminate events which include noise, multiple Compton interactions, or other types of interactions which are not simple Compton scatter events. Another cut selects only events for which the Compton scatter angle in Eq. (2) is physical ($-1 \leqslant \cos\theta \leqslant 1$). The set of events satisfying these two cuts (referred to as "imageable events" in the following text) are used to construct the back-projected image. After first reconstructing the back-projected image without any further cuts, a second step is used to reject some of the background. First, the algorithm searches for the largest peak in the backscatter image. Next, two deposited energy ($E_{tot} = E_{Si} + E_{CsI}$) distributions are created—one (the "source" energy distribution) for those events which pass within 5° of the peak in the image and another for all other events (the "background" energy distribution). The source energy distribution contains mainly events originating from the source, along with some background. The background energy distribution contains mainly events from background and from Compton scatter events in which some of the energy was not detected. The background energy distribution is subtracted from the source energy distribution to help isolate the energy peaks which originate from the source. Although this background subtraction method is imperfect, it is effective in isolating peaks associated with the source. The algorithm then searches for peaks in the background-subtracted distribution. The known energy resolution of the CsI (Eq. (1)) is used to look for peaks with the expected width—although the silicon detector energy resolution contributes to the overall energy resolution, it is a minor contribution. Multiple peaks may be found, depending on the source. Only events with total energies within 2σ (where σ is the value of FWHM from Eq. (1) divided by 2.35) of the center of one of the peaks are used to construct the final back-projected image. This algorithm does not assume that the identity of the source is known in advance. Making this cut in energy significantly reduces the background from events in which some of the energy escapes from the detector (invalidating Eq. (2)) and from background sources outside the region being imaged.
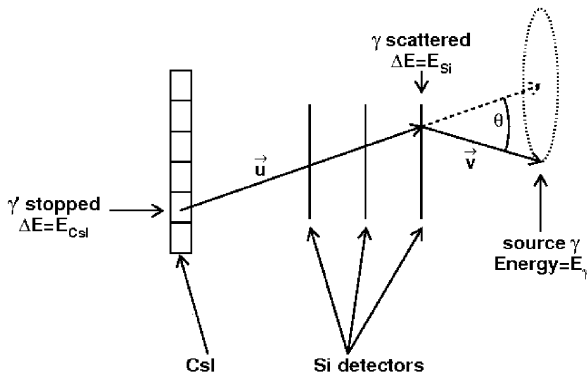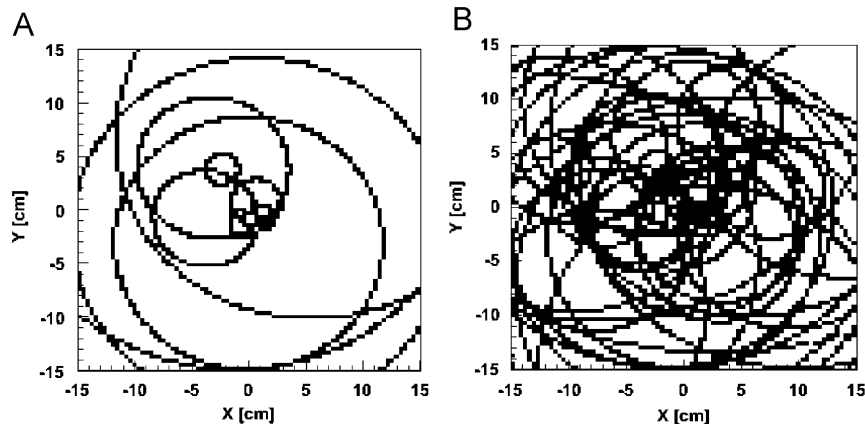

Fig. 2. A sketch of a sample Compton scattering interaction in the PCI showing the reconstruction cone. The arrows show the definitions of the vectors $\mathbf{u}$ and $\mathbf{v}$ defined in the text. The direction of travel of the photon is in the direction opposite to these two vectors (i.e. the photon travels from left to right in this sketch). Only the active parts of the detectors from Fig. 1 are shown. The initial position of the photon is labeled "source γ", the location of the Compton scattering event in the silicon is labeled "γ scattered" and the location at which the scattered photon is stopped in the CsI detector is labeled "γ stopped." The Compton scatter angle (θ) is shown. The dotted ellipse indicates the cone defined by the vector $\mathbf{u}$ and the Compton scatter angle.

Fig. 3. Back-projected image after 10 (A) and 50 (B) events for a simulated ^{137}Cs point source located at $(X = 0.0\,\text{cm}, Y = 0.0\,\text{cm}, Z = 10.0\,\text{cm})$. The source position becomes evident after a sufficient number of cones intersect.

In filling the back-projected image, there is a uniform angular distribution in ϕ—which correctly weights the cones which intersect the imaging plane at different angles. Here, this is implemented by using a series of equally spaced values of ϕ from 0 to 2π. In addition, because there is an uncertainty in the Compton scattering angle (from Eq. (2)) due to finite energy and position resolution, the algorithm estimates the uncertainty in the Compton angle and projects seven cones, with opening angles equally spaced between $\theta-2.4\sigma_\theta$ and $\theta+2.4\sigma_\theta$, where θ is the Compton scatter angle from Eq. (2) and σ_θ is the uncertainty in the angle. Each cone is given a weight based on the Gaussian probability for the given angle. Using more than seven cones slightly improves the image quality and using fewer cones increases the algorithm's speed—seven was chosen as a reasonable compromise between these competing effects. While the back-projection method works well for point-like source distributions like the one shown in Fig. 3, images created using this method make no correction for the variations of the sensitivity of the imager with position. Therefore back projection only works well for point sources—imaging of extended shapes requires a more advanced algorithm, such as maximum likelihood expectation maximization (MLEM) (Dempster et al., 1977).

4. List-mode maximum likelihood expectation maximization (LM-MLEM)

MLEM is an iterative statistical algorithm that uses successive approximations to determine the true source distribution given a set of data. The key equations used are Eqs. (4) and (5). The LM-MLEM method is a variation on the MLEM method that has been applied to the reconstruction of Compton images (Mihailescu et al., 2007; Zoglauer, 2005; Wilderman et al., 1998). In this paper the LM-MLEM method has been used. List-mode means that the set of data being used by the MLEM algorithm is simply a list of energy depositions and interaction points per event i.e. $I_0 = (E_{Si}, X_{Si}, Y_{Si}, Z_{Si}, E_{CsI}, X_{CsI}, Y_{CsI}, Z_{CsI})$ and reconstruction operates on each event one at a time. To start the process, a back-projected image, as described in the previous section, is created. Only events which are in the peaks in the deposited energy distribution, which have signals in exactly one silicon pixel and exactly one CsI detector, and which have for a Compton scatter angle which is physical ($-1 \leqslant \cos\theta \leqslant 1$) are used. The iterative equation for LM-MLEM is seen in Eq. (4) below, where λ_j^n represents the calculated amplitude of pixel j in the image at the nth iteration. The sensitivity function (S_j), which is described in detail in the next section, represents the probability that a gamma-ray originating from pixel j is detected anywhere in the PCI. The main summation is over all recorded event sequences $i = 1$, N which had a reconstruction cone intersecting pixel j. The weighted likelihood that event i originated from pixel j is t_{ij}. The secondary summation is over all pixels k intersected by the reconstruction cone of event i. Pixel weights are calculated from Eq. (5), where Δz is the thickness of CsI that a scattered photon would travel through given the vector $\boldsymbol{v}$ used in Eq. (3). The CsI interaction cross-section (σ_t) is at energy E_{CsI}, $\mathrm{d}\sigma_c/\mathrm{d}\Omega$ is the Klein–Nishina differential scattering cross-section evaluated at energy E_γ for the calculated scattering angle, R_{12} is the distance between the first and second interaction positions, and θ_{12} is the polar angle of the vector pointing from the scatter position to the absorption position.

$$\lambda_j^n = \frac{\lambda_j^{n-1}}{s_j} \sum_{i=1}^N \frac{t_{ij}}{\sum_k t_{ik}\lambda_k^{n-1}} \tag{4}$$

$$t_{ij} = \frac{\mathrm{d}\sigma_c}{\mathrm{d}\Omega} \frac{1 - \exp(-\sigma_t \Delta z)}{R_{12}^2 \cos\theta_{12}} \tag{5}$$

In (4) and (5) the first subscript in t_{ij} is an index for the event number ($i = 1, N$) and the second subscript (j) is an index for image pixels.

4.1. Sensitivity function calculation

The sensitivity function (S_j) is calculated analytically before imaging. It is the sum of the probabilities that a single event originating in the image pixel j will be detected anywhere in the PCI. The sensitivity is a function of three position variables (of the source location) and covers the anticipated imaging volume. It is calculated as the sum of the probability that a gamma-ray is emitted in the direction of the silicon times the probability that a gamma-ray survives the distance R_{01} (through air) from the image pixel to each of the 960 silicon pixels in the PCI. This is then multiplied by the sum of the probabilities that the gamma-ray will scatter in the thickness of silicon (ΔZ_{Si}) as seen from the image pixel. Next is the probability that the scattered gamma-ray will survive the distance R_{12} (through air) to each of the 42 CsI elements multiplied by the probability of scattering ($\mathrm{d}\sigma_c/\mathrm{d}\Omega$ from the Klein–Nishina formula) at the angle between the vectors formed by source to scatter position (V_{01} which is in the direction opposite the vector $\boldsymbol{v}$ shown in Fig. 2) and the scatter to absorption position (V_{12} which is in the direction opposite the vector $\boldsymbol{u}$ shown in Fig. 2) followed by the probability that the scattered gamma-ray will interact in the thickness of CsI (ΔZ_{CsI}) seen from the scattering position times the solid angle covered by the CsI crystal ($\approx A_{CsI} \cos\theta_{12}/R_{12}^2$). The formula for the calculation of the sensitivity function is shown in (6).

$$S_j = \sum_{Si} \left[\exp(-R_{01}/\Lambda_{air})(1 - \exp(-\Delta Z_{Si}/\Lambda_{Si})) \frac{A_{Si} \cos\theta_{01}}{4\pi R_{01}^2} \right.$$
$$\times \sum_{CsI} \left[\exp(-R_{12}/\Lambda_{air})(1 - \exp(-\Delta Z_{CsI}/\Lambda_{CsI})) \right.$$
$$\left. \left. \times \frac{\mathrm{d}\sigma_c}{\mathrm{d}\Omega} \frac{A_{CsI} \cos\theta_{12}}{R_{12}^2} \right] \right] \tag{6}$$

In (6), the solid angles covered by the Si and CsI detectors are approximated using the areas of the front surfaces of the Si and CsI pixels (A_{Si} and A_{CsI}, respectively). This is an excellent approximation for the thin silicon detectors and a reasonable approximation for the thicker CsI detector. Because the probability for photons to interact in the thin silicon detectors is small ($\Delta Z_{Si}/\Lambda_{Si} \ll 1$), an approximation ($1-\exp(-\varepsilon) \approx \varepsilon$ for $\varepsilon \ll 1$) can be used to slightly simplify (6) into the expression shown in (7). In these equations, T_{Si} is the thickness of silicon detectors (280 µm), Λ_{Si} is the interaction length in Si, Λ_{CsI} is the interaction length in CsI, and Λ_{air} is the interaction length in air. The interaction lengths are taken from Berger et al. (2005). Because only the shape of the function is important, not the overall normalization, the leading constants are omitted from the calculation during the imaging process.

$$S_j = \frac{T_{Si} A_{Si} A_{CsI}}{4\pi} \sum_{Si} \left[\exp(-R_{01}/\Lambda_{air}) \frac{1}{\Lambda_{Si} R_{01}^2} \right.$$
$$\left. \times \sum_{CsI} \left[\exp(-R_{12}/\Lambda_{air})(1 - \exp(-\Delta Z_{CsI}/\Lambda_{CsI})) \frac{\mathrm{d}\sigma_c}{\mathrm{d}\Omega} \frac{\cos\theta_{12}}{R_{12}^2} \right] \right] \tag{7}$$

Fig. 4 shows a sample section of the calculated sensitivity function for a slice at $Z = 10.0$ cm. At any fixed value of Z the maximum value for the sensitivity function is at ($X = 0$, $Y = 0$).

Thirty iterations were used for each of the images which followed—although images of extended sources did not change significantly after about 15 iterations. Point source images usually converge in 5–10 iterations. Unless otherwise noted, we have

shown the image from the last iteration. The imaging algorithm does not use a criterion to define convergence; the choice of thirty iterations to end the process was based on our experience. Adding an algorithm to define convergence is planned future improvement.

5. Results and comparison

5.1. Measured ^{60}Co point source

Fig. 5 shows a reconstructed image of data collected from a 337 kBq ^{60}Co point source. The PCI recorded 29,343 event sequences with the source located at ($X = 0.0$ cm, $Y = 3.0$ cm, $Z = 10.0$ cm) in the coordinate system defined in Fig. 1. Fig. 5 shows the difference between the back-projected source distribution (Fig. 5A) and the LM-MLEM reconstruction (Fig. 5B). It can be seen that both algorithms work for point source imaging.
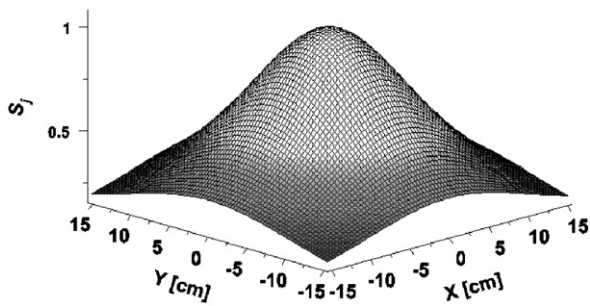

Fig. 4. Calculated sensitivity function at $Z = 10.0$ cm. Vertical axis (S_j) gives the normalized probability of detection. The probability of detection is largest (1.0) at ($X = 0$, $Y = 0$).
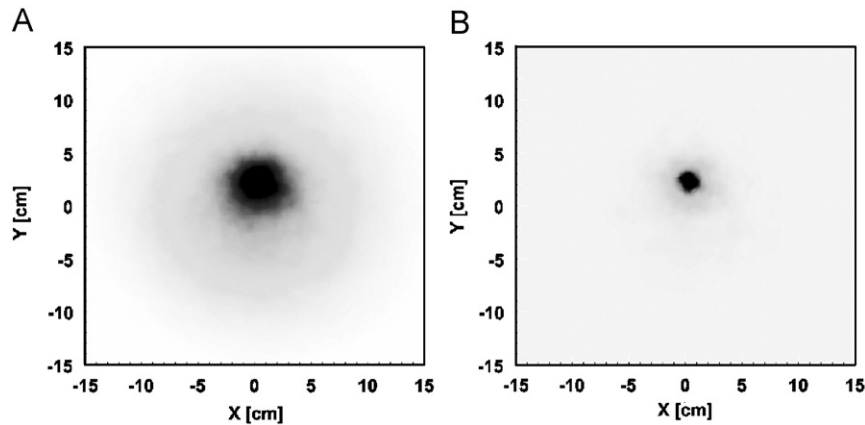
However, the LM-MLEM algorithm reduces image noise and produces a better quality image. Table 1 presents the solid angle subtended by reconstructed point images. The solid angle covered by the image is reduced by a factor of ~10 when switching from back projection to the LM-MLEM algorithm. The solid angle is measured from the center of the middle silicon plane.

5.2. Measured ^{137}Cs extended source ("L" source)

Extended source imaging with the PCI was performed using two different source distributions. The first test was to image an "L" shaped source. The length of the long (vertical) axis of the "L" was 12.7 cm, the length of the short (horizontal) axis was 5.0 cm, and the width of both the long and short axes was 1.3 cm. The source activity was 3616 kBq. The "L" source (Isotope, 2006) was located at $Z = 10.0 \pm 0.3$ cm. There were 275,987 recorded events. The system took approximately four days to collect this data set. Of the events that satisfied the hardware trigger condition, only 69,627 imageable events were used after energy cuts. The images in Fig. 6 show the difference between the back-projected source distribution reconstruction and the LM-MLEM reconstruction. The image to the left (Fig. 6) is constructed using the back-projection method described in Section 3. The middle and right images (Fig. 6) were reconstructed using the LM-MLEM method. The lines on the right image in Fig. 6 show the actual L source size and location. It is clear that the back-projection method is not adequate for extended source imaging.

Fig. 7 demonstrates the progress of LM-MLEM iterations for the data shown in Fig. 6. Image quality gets better as the number of iterations increases. Iterating past the point of convergence does not improve image quality. For this measured data set, processing was halted after 30 iterations.
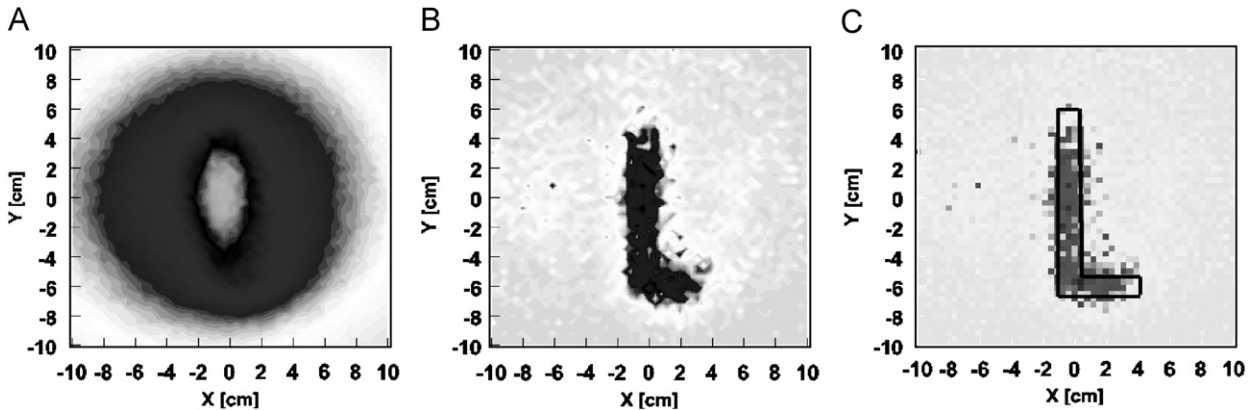

Fig. 5. A back-projected reconstruction of a measured ^{60}Co source at ($X = 0.0$ cm, $Y = 3.0$ cm, $Z = 10.0$ cm), after 29,343 events (A) and the same data after 10 iterations of LM-MLEM (B). The uncertainties on our X, Y and Z measurements in the laboratory were approximately 0.3 cm. The measurement took ~9.5 h.

Table 1
Energy-gated, back-projected, image resolution and after 10 iterations of LM-MLEM for various measured sources at various locations (X, Y, Z).

Source	Energy (keV)	(X, Y, Z) (cm)	Ω (Back-projection) (sr)	Ω (MLEM) (sr)	Ratio (BP/MLEM)
^{60}Co	1172, 1333	(0.0,3.0,10.0)	0.022	0.0021	10.48
^{54}Mn	834	(1.0,3.8,7.0)	0.012	0.0011	10.91
^{137}Cs	662	(1.0,3.8,7.0)	0.028	0.0029	9.66
^{137}Cs	662	(1.0,−3.0,10.0)	0.0077	0.00091	8.46

Any pixels in the image above 50% of the maximum single-pixel amplitude were considered part of the source. The image sizes are given in the solid angle (Ω) measured from the center of the middle silicon plane. The last column gives the ratio of the solid angles from the back-projection (BP) and LM-MLEM methods. Each image covered −15 cm to 15 cm in X and Y, with 81 pixels per axis. The uncertainties on our X, Y and Z measurements in the laboratory were approximately 0.3 cm.

Fig. 6. A back-projected reconstruction of ^{137}Cs "L" source using 69,627 imageable events (A), a LM-MLEM reconstruction of the same source after 30 iterations (B), and the same LM-MLEM image showing the actual source position (C). The differences between (B) and (C) reflect two different methods of displaying the same image. (B) shows contours and (C) shows pixel intensity.
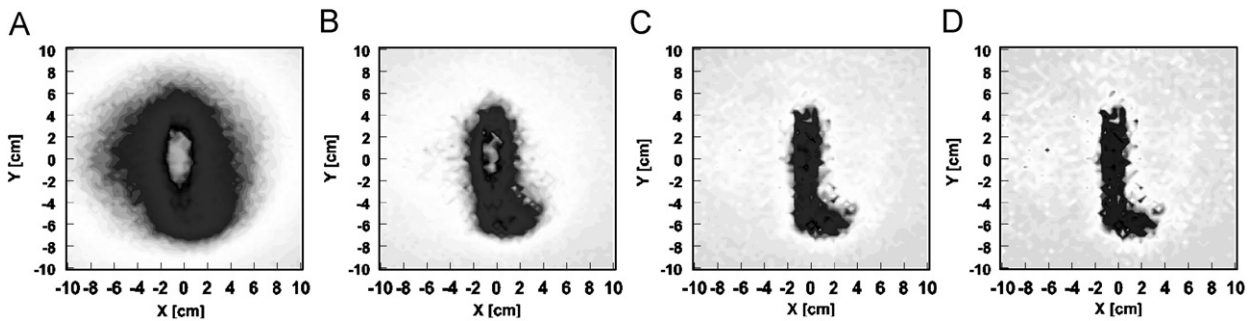

Fig. 7. The progression of LM-MLEM iterations for an "L" shaped ^{137}Cs source. The image after 1 (A), 5 (B), 15 (C), and 30 (D) iterations are shown. These images were generated from measured PCI data.
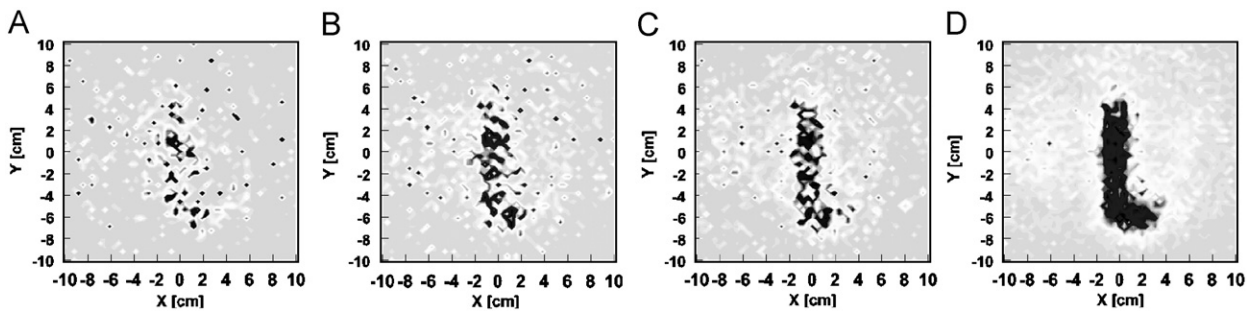

Fig. 8. Shows the change in the "L-source" image as the number of imageable events used is increased from 2000 (A), to 5000 (B), to 10,000 (C), to 69,627 (D). These images were generated from measured PCI data after 30 iterations of MLEM.

Fig. 8 shows the images that result when a subset of the events used to create the images in Fig. 7D are used. In Fig. 8, the four cases shown use 2000, 5000, 10,000, and 69,627 imageable events (after energy cuts). The image becomes better defined as the number of events used is increased. It is clear that 2000 events are insufficient and that 5000 events gives only a hint at the true shape. The true shape starts to become clear after 10,000 events and is quite clear after ∼70,000 events.

5.3. Measured ^{54}Mn ring source

A ring-shaped source was fabricated using a point source and a "propeller" attached to a motor which rotated the propeller at 1 rpm. The shaft of the motor was parallel to the Z axis in our coordinate system. The point source was attached to one end of the propeller and therefore, averaged over time, produced a ring-shaped source with the ring contained in a plane perpendicular to the Z axis. The image shown in Fig. 9 was generated using PCI data with a ^{54}Mn source mounted on the propeller. The idea to create a ring source with a motor and a propeller was proposed by Zoglauer (2005). The propeller swept out a circle with radius of 5.5 ± 0.2 cm. This approximated a radioactive ring source. The ring source was at $Z = 11$ cm. ML reconstructions (four iterations) of the measured and simulated "ring source" data are presented in Figs. 9 and 10, respectively. Fig. 9 also shows the back-projected image from the measurements with the ring source. The back-projected image shows a disk rather than a ring—as was previously shown by Zoglauer (2005). Using the LM-MLEM algorithm, the measured and simulated reconstructed images
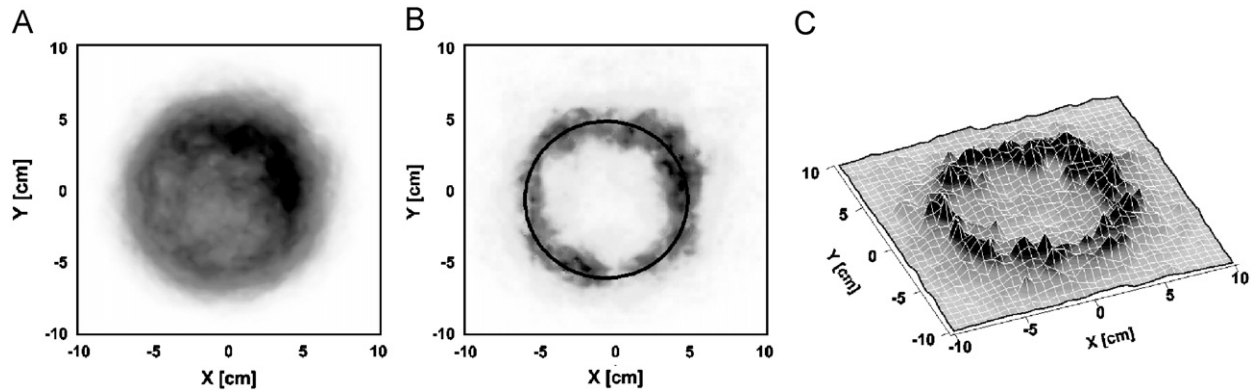
Fig. 9. Reconstruction of the measured ^{54}Mn ring source data: (A) shows the back-projection image, (B) shows the image after four iterations of LM-MLEM, and (C) shows the image from (B) in a "3D" plot. The circle drawn on (B) shows the actual location of the ring source. The center of the circle was at $X = -1$ cm and $Y = 0$ cm. The uncertainties on our X, Y and Z measurements in the laboratory were approximately 0.3 cm. The circle drawn has a radius of 5.5 cm. This image consists of 3014 imageable events after energy cuts (790 keV $< E <$ 910 keV). The data set took two days and 4 h to collect.
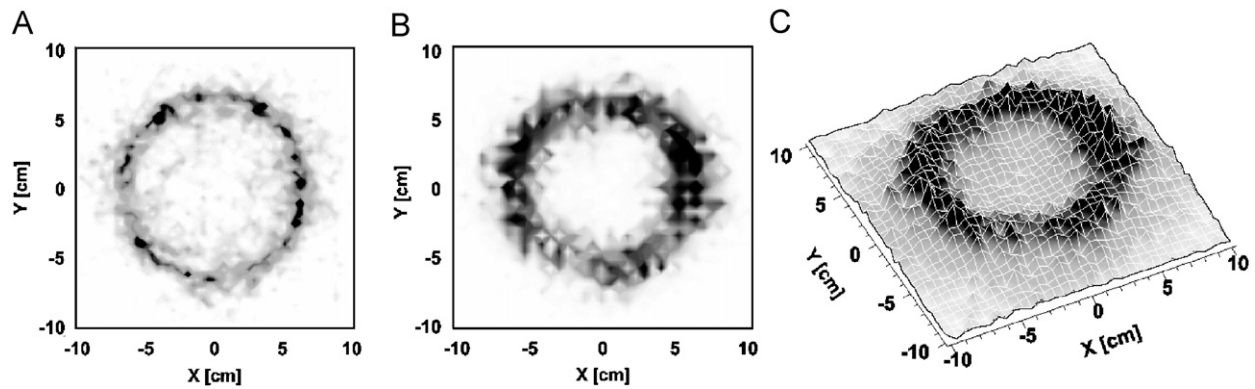

Fig. 10. Simulated ^{54}Mn ring source before (A) and after (B) energy and position resolution were added. (C) Shows a 3D representation of the ring source with resolution added. Images shown are after four iterations of LM-MLEM. The simulated images use 54,214 imageable events after energy cuts.

are similar and in both cases the ring-shaped image is reconstructed well. The width of the ring in the reconstructed image is approximately 3.4 cm FWHM. The diameter of the source itself is 0.5 mm—which is small compared to the width of the reconstructed ring. This width is because of the finite resolution of the PCI imager.

Fig. 10 compares an image from the reconstruction of simulated events. Fig. 10A shows the ring image which would result if the PCI had perfect energy and position resolution. Figs. 10B and C show the same image with the actual energy and position resolution of the PCI. The quality of the images in Figs. 10B and C are similar to the results from real data shown in Fig. 9.

6. Conclusions

The LANL PCI is a PCI that uses three Si planes (scattering planes) and a CsI(Tl) absorber plane. The PCI data was successfully used to image extended sources. We have shown reconstructed images using both the back-projection and LM-MLEM methods. It is evident that LM-MLEM is a superior algorithm for the reconstruction of both extended and point sources and that our simulations are in good agreement with the measured data. For example, the image of a point source is roughly a factor of 10 smaller (measured in solid angle, see Table 1) for the LM-MLEM algorithm than for the back-projection algorithm. Using the same data set from the PCI, the back-projection algorithm is unable to clearly show the shape of our "L" source, while the LM-MLEM

algorithm resolves it clearly. In fact, as shown in Fig. 8, the image could have been resolved with fewer events than we actually collected. Nevertheless, in some cases the PCI requires a long time to collect a sufficient data set for imaging of extended sources. That is because the silicon planes are thin (280 mm) and because the detector does not cover a large area. An operational detector would need to increase the detection efficiency by increasing some combination of the detection area and the detector thickness. As was shown with the MEGA detector (Zoglauer, 2005), the back-projection algorithm produces an image that looks like a disk using data from a ring-shaped source, but the LM-MLEM algorithm successfully resolves the ring image from the PCI with less than 4000 imageable events after energy cuts. The measurement results from the PCI indicate that a large imager based on the current prototype and algorithms will find successful use in counter terrorism and other applications.

References

Agonstinelli, S., et al., 2003. GEANT4—a simulation toolkit. Nucl. Instrum. Methods Phys. Res. Sect. A 506 (3), 250–303.

Berger, M.J., Hubbell, J.H., Seltzer, S.M., Chang, J., Coursey, J.S., Sukumar, R., Zucker, D.S., 2005. XCOM: Photon Cross Section Database (version 1.3). National Institute of Standards and Technology, Gaithersburg, MD. Available: ⟨http://physics.nist.gov/xcom⟩ (online, August 12, 2008).

Dempster, A.P., Laird, N.M., Rubin, D.B., 1977. Maximum likelihood from incomplete data via the EM algorithm. J. R. Stat. Soc. Ser. B (Methodol.) 39, 1–38.

Ideas, 2004. The readout electronics for the silicon detectors is based on the VA/TA chip series from IDEAS. The readout electronics (with the exception of the preamplifiers) for the CsI(TL) readout is based on custom circuit boards build

by IDEAS. The data were collected using the VATAC data acquisition system from IDEAS. ⟨http://www.ideas.no/welcome_more.html⟩.

Isotope, 2006. The source was made by Isotope Products ⟨http://www.ipl.isotopeproducts.com/new_ipl_site/⟩.

Kanbach, G., Andritschke, R., Zoglauer, A., Ajello, M., McConnell, M.L., Macri, J.R., Ryan, J.M., Bloser, P., Hunter, S., DiCocco, G., Kurfess, J., Reglero, V., 2005. Development and calibration of the tracking Compton/Pair telescope MEGA. Nucl. Instrum. Methods Phys. Res. Sect. A 541, 310322.

Kippen, R.M., 2004. The GEANT low energy Compton scattering (GLECS) package for use in simulating advanced Compton telescopes. New Astron. Rev. 48 (1–4), 221–225.

Kurfess, J.D., Novikova, E.I., Phlips, B.F., Wulf, E.A., 2007. Compton imager using room temperature silicon detectors. Nucl. Instrum. Methods Phys. Res. Sect. A 579, 367–370.

Lehner, C.E., He, Z., Zhang, F., 2004. 4π Compton imaging using a 3-D position-sensitive CdZnTe detector via weighted list-mode maximum likelihood. IEEE Trans. Nucl. Sci. 51, 1618–1624.

Li, 2001. The silicon pixel detectors were made under the direction of Zheng Li at Brookhaven National Lab, 2001.

Llosa, et al., 2008. Last results of a first Compton probe demonstrator. IEEE Trans. Nucl. Sci. 55, 936–941.

Mihailescu, L., Vetter, K.M., Burks, M.T., Hull, E.L., Craig, W.W., 2007. SPEIR: a Ge Compton camera. Nucl. Instrum. Methods Phys. Res. Sect. A 570 (1), 89–100.

Motomura, S., Enomoto, S., Haba, H., Igarashi, K., Gono, Y., Yano, Y., 2007. Gamma-ray Compton imaging of multitracer in biological samples using strip germanium telescope. IEEE Trans. Nucl. Sci. 54, 710–717.

Odaka, H., Takeda, S., Watanabea, S., Ishikawa, S.-N., Ushio, M., Tanaka, T., Nakazawa, K., Takahashia, T., Tajimac, H., Fukazawa, Y., 2007. Performance study of Si/CdTe semiconductor Compton telescopes with Monte Carlo simulation. Nucl. Instrum. Methods Phys. Res. Sect. A 579, 878–885.

Park, S.J., Rogers, W.L., Huh, S., Kagan, H., Honscheid, K., Burdette, D., Chesi, E., Lacasta, C., Llosa, G., Mikuz, M., Studen, A., Weilhammer, P., Clinthorne, N.H., 2007. Performance evaluation of a very high resolution small animal PET imager using silicon scatter detectors. Phys. Med. Biol. 52, 2807–2826.

Rawool-Sullivan, M.W., Sullivan, J.P., Tornga, S.R., Brumby, S.P., 2008. A simple algorithm for estimation of source-to-detector distance in Compton imaging. Appl. Radiat. Isot., doi:10.1016/j.apradiso.2008.06.040.

Riberfors, R., 1975. Relationship of the relativistic Compton cross section to the momentum distribution of bound electron states. Phys. Rev. B 12, 2067.

St. Gobain, 2003. The 42-element CsI(Tl) detector array, along with the photodiodes and preamplifiers attached to them, was built by St. Gobain crystals ⟨http://www.bicron.com⟩.

Takeda, S., et al., 2007. A new Si/CdTe semiconductor Compton camera developed for high-angular resolution. In: Proceedings of the Society of Photo-Optical Instrumentation Engineers (SPIE), vol. 6706, pp. 67060S-1–67060S-10.

Vetter, K., Burks, M., Cork, C., Cunningham, M., Chivers, D., Hull, E., Krings, T., Manini, H., Mihailescu, L., Nelson, K., Protic, D., Valentine, J., Wright, D., 2007. High-sensitivity Compton imaging with position-sensitive Si and Ge detectors. Nucl. Instrum. Methods Phys. Res. Sect. A 579, 363–366.

Wilderman, S.J., Clinthorn, N.H., Fessler, J.A., Les Rodgers, W., 1998. List-mode maximum likelihood reconstruction of Compton scatter camera images in nuclear medicine. IEEE Nucl. Sci. Symp. Conf. Rec. 3, 1716–1720.

Zoglauer, A., 2005. Ph.D. Thesis, TU Munich. Available from: ⟨http://www.mpe.mpg.de/MEGA/documents/thesis/PhD_AndreasZoglauer.pdf⟩.